ADVANCED ENERGY MATERIALS
www.advenergymat.de

Atomic-Scale Revealing the Structure Distribution between $LiMO_2$ and Li_2MnO_3 in Li-Rich and Mn-Based Oxide Cathode Materials

Haoxiang Zhuo, Haoyang Peng, Biwei Xiao, Zhenyao Wang, Xingge Liu, Zhao Li, Guohua Li, Xiangtao Bai, Ligen Wang, Xiaowei Huang, Jingsong Wu, Wei Quan, Jiantao Wang, Weidong Zhuang,* and Xueliang Sun**

Lithium-rich and manganese-based oxide (LRMO) cathode materials are regarded as promising cathode materials for lithium-ion batteries with anionic redox characteristics and higher specific energy density. However, the complex initial structure and complicated reaction mechanism of LRMO is controversial. Herein, the reaction mechanism and unusual electrochemical phenomena are reconsidered after proposing the concept of structure distribution between Li_2MnO_3 and $LiMO_2$ structures. The initial structure states show different types of composition characteristics of Li_2MnO_3 and $LiMO_2$, including "large and isolated distribution" and "uniformly dispersed distribution" characteristics, as summarized by multiple aberration correction scanning transmission electron microscopy observations at the atomic-scale for cross sectional samples. Based on the density functional theory calculations, X-ray absorption spectroscopy, and atomic-scale observations during the different voltage states, the results accordingly suggest that the distribution characteristic is the essential cause of the unusual behavior in LRMO. It governs the reaction behavior, leading to the changes in electronic structure of O_{2p} and TM_{3d}, and the maintenance of layered structure, reversibility of the anionic redox, as well as, the voltage hysteresis. This work constructs the interrelationships of electrochemical behavior—distribution characteristic—reaction mechanism, contributing to the further application of LRMO materials in the electric vehicle market.

1. Introduction

In recent years, lithium-ion batteries (LIBs) have gradually taken over various areas in life and started to dominate transportation with the demand for environmental protection and human daily activities. Lithium-ion electric vehicles (EVs) are considered to be an extremely important means of transportation.[1] The eternal pursuits of LIBs are long-range and low cost. However, the current commercial cathode materials that exhibit high cost and low capacity are not suitable for the EVs markets. Lithium-rich and manganese-based oxides (LRMO) cathode materials are considered to be an ideal choice for next-generation LIBs since they can meet the demand for ultra-high specific energy while being environmentally friendly and low-cost.[2–5]

LRMO, which can be written as $xLi_2MnO_3{\cdot}(1\text{-}x)LiMO_2$ (M = Ni, Co, and Mn, $0 < x < 1$), has attracted many researchers for the complex structure composition and unusual electrochemical reaction mechanism. LRMO is capable of

H. Zhuo, B. Xiao, Z. Wang, X. Liu, G. Li, X. Bai, W. Quan, J. Wang
China Automotive Battery Research Institute Co., Ltd.
Beijing 100088, China
E-mail: wangjt@glabat.com

H. Zhuo, B. Xiao, X. Liu, G. Li, J. Wang
National Power Battery Innovation Centre
GRINM Group Co., Ltd.
Beijing 100088, China

The ORCID identification number(s) for the author(s) of this article can be found under https://doi.org/10.1002/aenm.202203354.

DOI: 10.1002/aenm.202203354

H. Zhuo, B. Xiao, Z. Wang, X. Liu, G. Li, X. Bai, L. Wang, X. Huang, W. Quan, J. Wang, W. Zhuang
General Research Institute for Nonferrous Metals
Beijing 100088, China

H. Peng, J. Wu
State Key Laboratory of Advanced Technology for Materials Synthesis and Processing & Nanostructure Research Centre
Wuhan University of Technology
Wuhan, Hubei 430070, China

B. Xiao
GRINM (Guangdong) Institute for Advanced Materials and Technology
Foshan, Guangdong 528051, China

Z. Li
National Engineering Research Center of Light Alloy Net Forming & State Key Laboratory of Metal Matrix Composite
Shanghai Jiao Tong University
Shanghai 200240, China

delivering ultra-high specific capacity of more than 300 mAh g^{-1} under high voltage (>4.5 V)[6] attributed to the redox reaction of lattice oxygen, which is completely different from the cationic redox of conventional cathode materials.[7,8] The essential origin of the redox reaction from the lattice oxygen is the unhybridized or non-bonding O2p states, which are distributed along the Li—O—Li configuration, and the non-bonding O2p states react independently of other Transition Metal (TM) orbitals, thus exhibiting the anionic redox character.[7] And the Li—O—Li configuration arises from the distribution of the additional Li ions that appear in the TM layer. The reaction mechanism of LRMO materials with some strange behavior of anionic redox has been investigated, but the related underneath mechanism remains under-explored. For example, the mechanism that maintains the reversible anionic redox as well as the transition of lattice oxygen during the charging and discharging states. After the first charge activation, the anionic reaction is spread over multiple voltage ranges, especially in the lower voltage range.[9] In addition, voltage hysteresis, voltage decay, and structure collapse have shackled the further development of LRMO cathode materials for a long time, and the structure transformation during lithium (de)intercalation has been the subject of long-standing controversy, spurring researchers to investigate the nature.[10–15]

Experience in the synthesis of LRMO materials indicated that the nuance in the synthesis condition was bound to lead to electrochemical differences. The hidden reason is the changes in the arrangement inside the LRMO particles, especially at the atomic-level, caused by the changes in the synthesis conditions. Meng et al. pointed out that the changes in the synthesis conditions significantly affected the structure and even the electrochemical properties of LRMO.[16] The delocalized LiMn6 superstructure has a great influence on the electrochemical reaction behavior of LRMO.[17,18] In addition, LRMO possesses a complex initial structure, and the composition of Li_2MnO_3 and $LiMO_2$ structures makes the distribution of the material at the atomic-scale confusing.[19] Yu et al. made a systematic and detailed study of the initial structure for LRMO materials and proposed the concept of domains, suggesting that the interaction of twin domains formed by the Li_2MnO_3 and $LiMO_2$ phases, respectively, is fundamental to the composition of the particle structures.[20,21] Abraham et al. observed that the Li_2MnO_3-like and $LiCoO_2$-like appeared homogeneous over the long-range in $Li_{1.2}Co_{0.4}Mn_{0.4}O_2$.[22]

However, the distribution model of Li_2MnO_3 and $LiMO_2$ structures within the domains of the particles needs to be investigated in-depth and comprehensively, from the atomic-scale observation to the electronic structure and up to the connection of the reaction mechanism, and whether there are multiple ways to composite the two at the nanoscale is uncertain. In this work, the concept of structure distribution has been proposed. The reaction mechanism of LRMO cathode materials has been reconsidered from the perspective of the composition of Li_2MnO_3 and $LiMO_2$ structures at the nano-scale, and it was found that a series of reaction behaviors of LRMO materials such as reaction activity, the reversibility of anionic redox, and even voltage hysteresis were closely related to the structure distribution. Different ways of distribution "large and isolated distribution" and "uniformly dispersed distribution" have been proposed by multiple aberration correction scanning transmission electron microscopy (AC-STEM) observations from atomic-scale after the treatment of focused ion beam (FIB) for particles. Based on the electrochemical measurement, density functional theory (DFT) calculations, X-ray absorption spectroscopy (XAS), and AC-STEM observations during the different states of lithium (de)intercalation, it was confirmed that the uniformly dispersed distribution of Li_2MnO_3 and $LiMO_2$ has brought a radical change to LRMO materials, which affects the non-bonding 2p state of oxygen, and increased the electrochemical reactivity. Moreover, as the deintercalation of lithium continues, the expansion of the interlayer spacing in the $LiMO_2$ structure, in turn, influenced the interlayer spacing in the Li_2MnO_3 structure that blends with it, thus improving the ability of the lithium ions deintercalation. In addition, voltage hysteresis was found to be highly correlated with the anionic reversibility. The introduction of the concept of distribution can explain the maintenance of the layered structure and the reversibility from oxidation to reduction upon lattice oxygen, and is one of the causes of voltage hysteresis by the changes in the electronic states.

2. Results and Discussion

2.1. Observation of Different Structure Distribution

The synthesis conditions have a huge influence on the local structure as has been mentioned in lots of works.[18,23,24] The general rule for the influence of synthesis conditions on the distribution of Li_2MnO_3 and $LiMO_2$ structures is being investigated systematically in another work, where the synthesis conditions are varied in terms of calcination temperature, annealing time, atmosphere, and Li: TM ratio. In this research, the distribution states of the two structures were regulated by simply changing the synthesis conditions. Taking $0.5Li_2MnO_3$-$0.5LiMn_{1/3}Ni_{1/3}Co_{1/3}O_2$ ($Li_{1.2}Mn_{0.54}Ni_{0.13}Co_{0.13}O_2$) as the benchmark, three types of samples L0 (1.20: 0.8), L3 (1.164: 0.8), and L5 (1.14: 0.8) with different degrees of dispersion of the structures were obtained by slightly changing lithium content, that is, Li:TM ratio, while ensuring other synthesis conditions were completely consistent. Inductively coupled plasma atomic emission spectrometry was employed to identify the chemical compositions of the three pristine powders. The mass ratios of Li, Mn, Ni, and Co of the samples are listed in the Table S1, Supporting Information, and the mass ratios were converted to atomic ratios and "normalized" with (Mn + Ni + Co) = 0.8 in order to facilitate identification. As shown in Table S1, Supporting Information, the elemental components of the three samples are basically consistent with the designed chemical components.

The three samples were studied to confirm differences in dispersion and distribution. The Li_2MnO_3 structure is a stack of—layer O—layer Li—layer O—layer $LiMn_2$—layer O. In the

W. Zhuang
Beijing Key Laboratory of Green Recovery and Extraction of Rare and Precious Metals
University of Science and Technology Beijing
Beijing 100083, China
E-mail: wdzhuang@ustb.edu.cn
X. Sun
Department of Mechanical and Materials Engineering
University of Western Ontario
London, Ontario N6A 5B9, Canada
E-mail: xsun9@uwo.ca

$LiMn_2$ layer, Li and Mn are arranged in a honeycomb-like order (Li−Mn−Mn), and this type of ordered arrangement leads to the unique superlattice diffraction of Li_2MnO_3 in the X-ray diffraction (XRD) patterns (20°–35°), which is a sign of LRMO materials. Breaking the long-range order of this superlattice structure causes a broadening of the superlattice peaks and a decrease in diffraction intensity. The XRD patterns (Cu kα) of the three samples are shown in **Figure 1**a, followed by the normalized processing according to the strongest peak ((003) around 19°). The intensity and profile of the main diffraction peaks are almost identical for each sample, all of which can be indexed to *C*2/*m*-Li_2MnO_3 or R-3m-$LiMO_2$. However, the superlattice peaks become weaker and wider from L0 to L3 to L5, presenting a trend in the distribution characteristics. The integration values superlattice peaks (20°–30°) from L0 to L3 to L5 were 0.826, 0.0723, and 0.0343, respectively, which showed a trend of weakening superlattice peaks. In order to verify the influence of the large isolated distribution or uniformly dispersed distribution on the profile of the superlattice peak, several models were constructed to simulate the XRD patterns by DIFFaX. The same amount of Li_2MnO_3 and $LiMO_2$ were adopted for simulating, that is, $0.5Li_2MnO_3$-$0.5LiMO_2$, as shown in Figure S1a, Supporting Information, when the distribution was large and isolated, that is, $LiMn_2$-$LiMn_2$-$LiMn_2$- ... -$LiMn_2$-TM-TM-TM- ... -TM (for simplicity, the Li and O layers are omitted), the profiles of the superlattice peaks were not greatly affected and still possessed the strong diffraction intensity. When the two were uniformly mixed and dispersed, that is, $LiMn_2$-TM-$LiMn_2$-TM-...-$LiMn_2$-TM-, the superlattice peaks were accompanied by broadening and weakening while the other peaks remain consistent, in agreement with the experimental XRD curves. It is suggested that the changes in the distribution properties of Li_2MnO_3 and $LiMO_2$ structures greatly affect the long-range order and thus change the diffraction patterns.

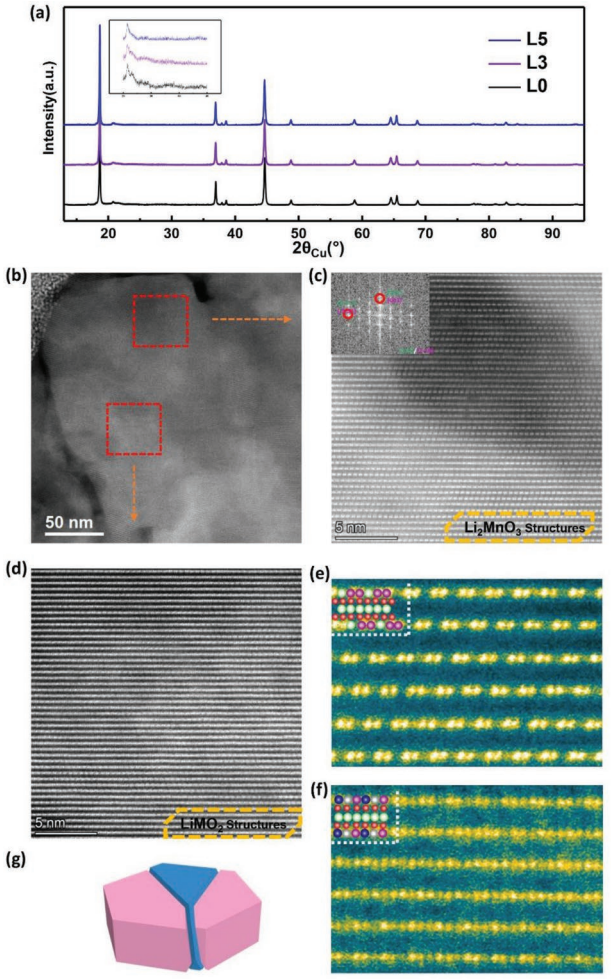

Figure 1. a) XRD (Cu-Kα) curves XRD curves for three samples with different structure distribution characteristics with background correction and the normalized processing according to the strongest peak ((003) around 19°), inset is enlarged view of the superlattice peaks. Original XRD patterns were shown in Figure S5, Supporting Information. b) Large-scale HAADF-STEM image for sample L0, showing the whole particle after FIB treatment. c) HAADF-STEM atomic-scale imaging of the Li_2MnO_3 structure in the particles, corresponding to the randomly selected region in (b) with above red boxed lines, showing the isolated distribution of almost all the Li_2MnO_3 structures. Inset image is the fast Fourier transform of the atomic image in (c). d) HAADF-STEM atomic-scale imaging of the $LiMO_2$ structure in the particles, corresponding to the randomly selected region in (b) with red boxed lines below, showing the isolated distribution of almost all the $LiMO_2$ structures. e) Enlargement of the atomic image of Li_2MnO_3 structures, the inset image shows the structure model of Li_2MnO_3. f) Enlargement of the atomic image of $LiMO_2$ structures, the inset image shows the structure model of $LiMO_2$. g) Schematic model for the particle with large and isolated distribution

It was estimated that the structure distribution of L0, L3, and L5 samples showed a trend from isolated to dispersed distribution. Employing the profile and intensity of the superlattice peaks is not accurate enough to identify the distribution characteristics of the structure and are not unique, it was only a qualitative means to determine the tendency of distribution characteristics. To further confirm the atomic arrangement, STEM was applied after FIB treatment for sample slices, and the local structures in the bulk were revealed. For high-angle annular dark field (HAADF)—STEM image, light elements such as Li and O present dark spots, while heavy elements such as TM present bright spots,[20,25] and the -dark-bright-bright-dark-bright-bright- arrangement corresponds to the $LiMn_6$ arrangement in the Li_2MnO_3-like structure (−Li−Mn−Mn−Li−Mn−Mn−), while the -bright-bright-bright-spot arrangement corresponds to the continuous arrangement of -TM-TM-TM- in the $LiMO_2$-like structure. Therefore, the atomic-scale HAADF-STEM observation along the [100] zone-axis is an efficient tool to distinguish the degree of dispersion and distribution between the Li_2MnO_3 and $LiMO_2$. For sample L0, which is predicted to present a large and isolated distribution, we selected regions far apart in the same particle for comparison and obtained two types of atomic arrangements that are completely different from each other in Figure 1b. As shown in Figure 1c,e, Region 1 of the L0 particle was almost filled with Li_2MnO_3 structures, accompanied by very few continuous arrangements of TM, and the corresponding fast Fourier transform exhibited pure *C*2/*m* structures. Region 2, on the other hand, was almost composed of the $LiMO_2$ structure (Figure 1d,f). Thus, the structures of Li_2MnO_3 and $LiMO_2$ in this special sample L0 crystallized separately in a large region.

As for sample L5 (**Figure 2**), the homogeneous mixing of Li_2MnO_3 and the $LiMO_2$ arrangement was almost ubiquitous

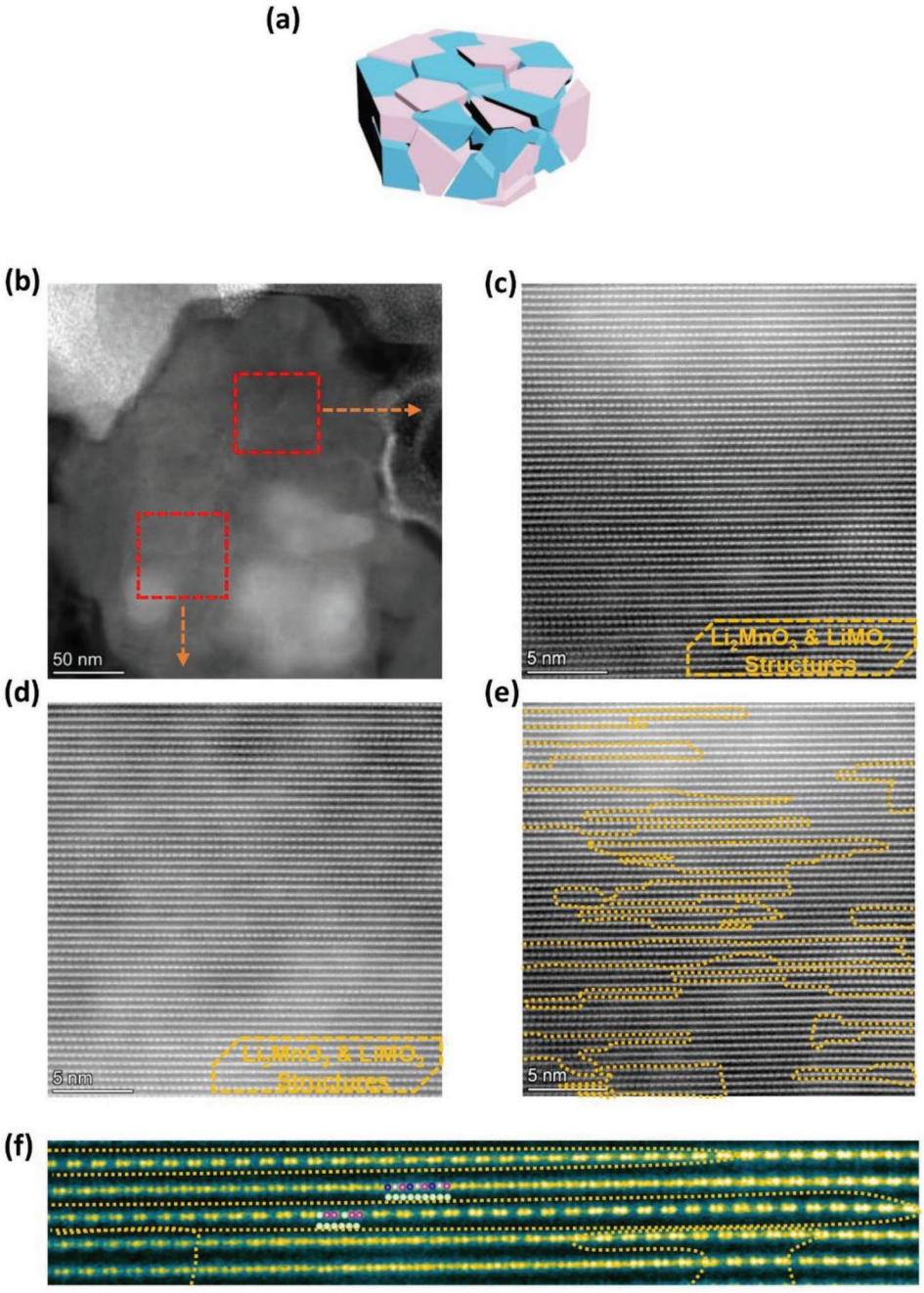

Figure 2. a) Schematic model for the particle with uniformly dispersed distribution. b) Large-scale HAADF-STEM image for sample L5, showing the whole particle after FIB treatment. c,d) HAADF-STEM atomic-scale imaging, corresponding to the randomly selected region in (b) with red boxed lines, showing the nanoscale dispersed distribution of Li_2MnO_3 structure and $LiMO_2$ structures. e) Li_2MnO_3 structures and $LiMO_2$ structures are distinguished by the yellow dashed line, and the Li_2MnO_3 structures are inside the box. f) Enlargement of the atomic image in (d), the inset image shows the structure model of Li_2MnO_3 and $LiMO_2$.

in various regions. To show that this is a general phenomenon, HAADF images (Figure 2c,d) of several regions in the particles were randomly selected, showing a uniformly dispersed distribution of Li_2MnO_3 and $LiMO_2$ structures, with the $LiMn_2$ and TM layers alternating almost once every few atomic layers or ≈1 nm. In the STEM images along the [100] zone axis, the $LiMnO_2$ phase is distinguished from the Li_2MnO_3 by the extra dots as indicated in Figure 2e,f, which are due to the replacement of Li by Mn. However, as the heterogeneous structure of the two phases is 3D, a quantitative analysis may have an error, especially in the adjacent areas of the two phases. In this work, we performed qualitative analysis on the deconvolution of the domain distribution to support the major conclusions. As shown in Figure 2e, the distribution of the two types of structures was distinguished by the yellow dashed line at the nanoscale, with the Li_2MnO_3 structure and $LiMO_2$ structure

inside and outside the dashed line, respectively. Thus, the uniformly dispersed distribution of these two structures is not only limited to the stacking along the c-direction but also exists within the same layer of the a-b plane.

2.2. Fundamental Influence of Structure Distribution Characteristics on the Electrochemical Behavior of Lithium-Rich and Manganese-Based Oxide

The changes in the distribution characteristics affect the intergrowth between Li_2MnO_3 and $LiMO_2$ structures within the particles at the nano-scale. The long-range ordered atomic arrangements are rendered to be changed when the two structures are dispersed in the particles, and the complex short-range local structure is bound to bring great variability in the reaction behavior, and is even the essential cause of electrochemical phenomena. As shown in **Figure 3**a, the charge-discharge curves during the first cycle of the three samples showed great differences between each other. As the Li_2MnO_3 structure became more dispersed in the particles, the first-charge capacity was gradually increased from sample L0 to L5, where the first charging plateau was then lengthened substantially. The first charging plateau at ≈4.5 V corresponds to the charge compensation of the non-bonding O 2p states in the Li_2MnO_3 structure, which is an important feature of the anionic oxidation in the LRMO material.[6] It indicated that the dispersed distribution of Li_2MnO_3 contributes to the improvement of lattice oxygen activity in LRMO. As shown in Figure S2a, Supporting Information, the increase in first charge capacity was basically from the capacity increase in lattice oxygen reaction (>4.4 V).

In LRMO materials, the evolution of lattice oxygen after the first charge includes: Part of the oxygen continues to participate in the reduction reaction stably during the discharge process in the form of intermediate; while the other part releases as oxygen gas. Generally, the longer the charging plateau of oxygen, the higher the first charging capacity, which corresponds to more oxygen gas evolution. However, as shown in Figure 3a, the higher charging capacity corresponds to a higher discharge capacity, that is, the first coulomb efficiency has been greatly improved as the two structures become more dispersed in the particles (as shown in Figure S2b, Supporting Information), which seemed counterintuitive. It could be further observed from the dQ/dV curves (Figure 3b) that the increase in the reversibility of charging and discharging (or called oxidation and reduction reversibility), derive from the capacity boost in the voltage range of about 3.0–3.5 V in discharge, which was the manifestation range of the voltage hysteresis behavior from lattice oxygen. Therefore, the dispersed distribution not only enhanced the activity of lattice oxygen, but also improved its redox stability as well as the voltage hysteresis phenomenon. Following part details how the change in the distribution characteristics affects the electrochemical behavior above from atomic to electronic structure.

The most immediate consequence of the dispersed mixing of the two structures is the generation of a large number of "phase-like interfaces," that is, the composite interfaces between the Li_2MnO_3 structure and the $LiMO_2$ structure after the intergrowth at nanoscale. Although the structures of Li_2MnO_3 and $LiMO_2$ are extremely similar, these interfaces resulted from the composite of the two structures cause abnormal adjacent coordination structures to appear, which are different from the internal arrangement of the two structures. Besides, the more dispersed the two structures are in the particles, the more phase-like interfaces there are. There are two kinds of phase-like interfaces, namely, two simplified composite modes, which are summarized in detail by HAADF-STEM images of the dispersed distribution. Phase-like interfaces A: The Li_2MnO_3 and $LiMO_2$ structures are mixed and stacked along the c-direction (Figure S3a,b, Supporting Information); Phase-like interfaces B: Compositing within the a-b plane, that is, the -$LiMn_2$-$LiMn_2$-$LiMn_2$- and -TM-TM-TM- arrangements appear in the TM layer simultaneously (Figure S3c,d, Supporting Information).

2.2.1. Facilitation of Reaction Activity

The O K-edge soft X-ray absorption spectroscopy (sXAS) was obtained to confirm the oxygen reactivity. The pre-edge peaks at ≈529 eV and ≈532 eV correspond to the transition of O 1s electrons to the empty TM 3d-O 2p hybrid orbital together with the 2p states of O,[26] and the changes in the integrated intensity of pre-edge peaks during the charging process correspond to the charging activity of lattice oxygen.[27] For sample L5 with dispersed distribution, as shown in **Figure 4**d,e, the integrated intensity and profile of the pre-edge peaks were relatively similar between the pristine state and the charged 4.4 V state. While from the 4.4 V state to the 4.8 V state, the integral intensity of the pre-edge increased sharply, corresponding to the strong reaction of the lattice oxygen. In contrast, sample L0 with isolated distribution characteristic did not show as much variation in integral intensity as sample L5 during the charging process, although it also possessed oxygen oxidation activity (Figure S4a, Supporting Information). It indicated that the increase in reactivity caused by the change in distribution characteristics can be partly attributed to the activation enhanced of 2p states from lattice oxygen. In addition, as shown in Figure S4b, Supporting Information, the Mn L-edge sXAS spectra of pristine states for all three samples exhibited Mn^{4+}, which excluded the presence of low-valent Mn in the powder as well as the spinel structure. At the same time, the sXAS spectra of the Mn L-edges in different delithiation states all showed the Mn^{4+} state (Figure S4c, Supporting Information), which further excluded that the improvement of reaction activity comes from the valence changes in Mn.

DFT calculations were introduced to demonstrate the changes in the electronic structure and the improvement of the oxygen activity when Li_2MnO_3 and $LiMO_2$ were combined in the above two ways, and the models were constructed based on the observed from STEM-HAADF. It is known that the redox reactions during charging and discharging correspond to the loss and gain of the electrons in the cathode material, namely the loss of occupied states and the filling of unoccupied states, respectively. The energy level distribution of occupied states in the pre-delithiated structure determines the order of the oxidation reaction and the charging voltage due to the corresponding relationship with the lithium metal orbitals. For LRMO cathodes, the reaction during the lower voltage range

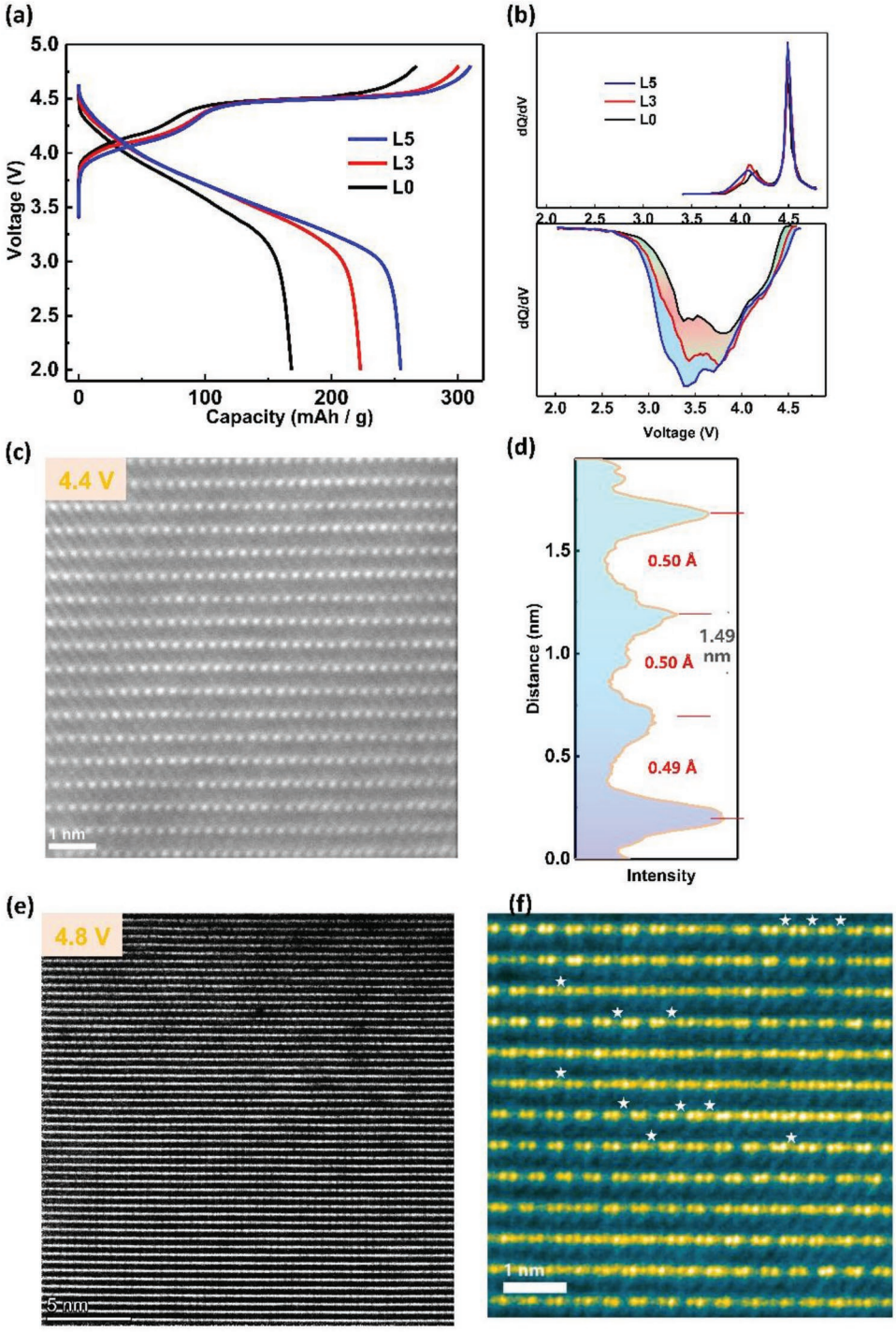

Figure 3. a) First charge/discharge curves of three samples (2–4.8 V, 20 mA g^{-1}). b) The *dQ*/*dV* curves corresponding to the first charge/discharge curves. c) HAADF-STEM image for sample L5 in the first charging 4.4 V state. d) Interlayer spacing for atomic image in (c). e) HAADF-STEM image of a larger range for the sample L5 in the bulk at the charging 4.8 V states, showing the relatively perfect layer structures. f) Enlarged HAADF-STEM image of the sample L5 in the bulk charged at 4.8 V, the asterisks indicate the TM ions of partial in-plane migration in the Li_2MnO_3 structure.

(<4.5 V) corresponds to the oxidation of Ni e_g orbital closer to the Fermi level with Co t_{2g} orbital, that is, the delithiation in the $LiMO_2$ structure. While ≥4.5 V corresponds to the non-bonding O2p states of Li_2MnO_3, which is slightly farther than the Fermi level but isolated from the other TM orbitals.[7,8]

The partial density of states (pDOS) of O in the Li_2MnO_3 structure was shown in Figure 4b, the 2p orbitals near the Fermi level were the non-bonding O2p states around Li—O—Li, which was the origin of the high capacity and anionic redox. When composited with the Li_2MnO_3 in the form of "phase-like

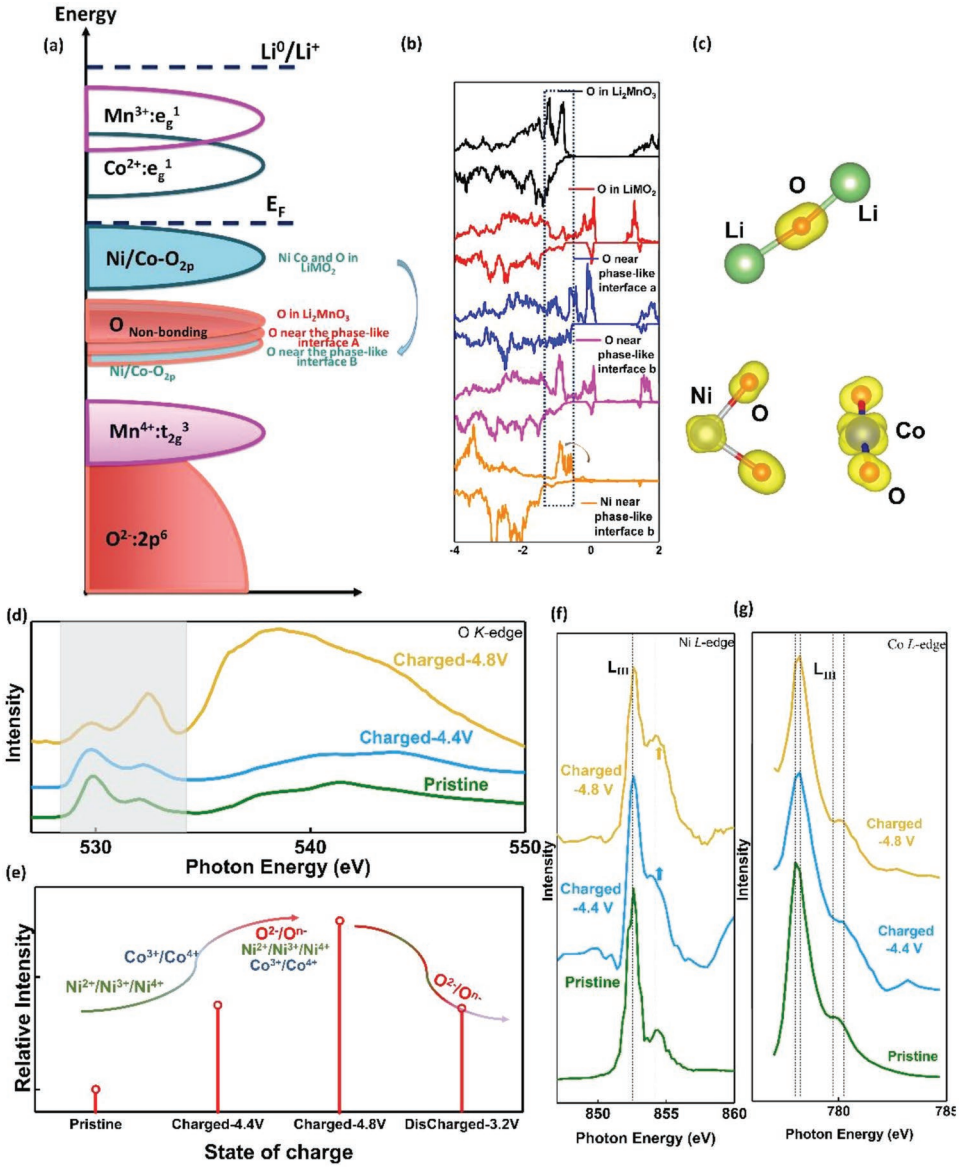

Figure 4. a) Schematic diagram of the electronic structures of various complex structures formed after the dispersed composite of Li_2MnO_3 structure and $LiMO_2$ structure. b) O pDOS in different local environments and pDOS of Ni near the interface B. c) Partial charge density diagram for slightly lower energy range (–1.5—0.5 eV) around O in Li_2MnO_3 structure, Ni and Co near the "phase-like interfaces B." d) O K-edge sXAS spectra with different delithiation states (TEY mode). e) Variation of the normalized integrated intensity for the O K-edge pre-edge peaks of sample L5 under different charging and discharging states, and the diagram of multiple redox pairs reacting in different voltage ranges. f) Ni L-edge sXAS spectra with different delithiation states of sample L5. g) Co L-edge sXAS spectra with different delithiation states of sample L5.

interfaces A," the O 2p states near the interface in $LiMO_2$ exhibited special features. As shown in Figure 4a,b, in addition to the higher occupied states that are coordinated to Ni and Co, a part of the special non-bonding 2p states in the slightly lower energy range, which overlaps with the energy range of the non-bonding O2p states in Li_2MnO_3, implying that the $LiMO_2$ structure is also partially involved in the oxidation of lattice oxygen at the high voltage of ≈4.5 V.

While near the "phase-like interfaces B," the composition within the a-b plane makes the situation even more different. As shown by the pDOS of O in Figure 4a,b, the 2p states of O in $LiMO_2$ near the "phase-like interfaces B" split partly to a relatively low energy range that almost overlaps with the energy range of the non-bonding O 2p states in Li_2MnO_3 structures. It should be noted that, unlike Li_2MnO_3, these low-energy O2p states in $LiMO_2$ are not non-bonding. The pDOS of Ni (Figure 4b) showed that in this case the Ni e_g states transfer to the lower energy range, which should have been in the range closest to the Fermi level, and they overlap with those O 2p states reduced energy in $LiMO_2$, forming the relatively lower energy Ni_{eg}-O and Co t_{2g}-O bonds, respectively (Figure 4a,b). As shown in Figure 4c, the partial charge density diagram for the energy ranges visualized that in the slightly lower energy range (–1.5 eV—0.5 eV), the charge distribution exists simultaneously

in O of Li_2MnO_3 and O, Ni, and Co in $LiMO_2$, together with Ni and Co forming the σ or π-type overlap with the O near the "phase-like interfaces B." While in the higher energy range, the charges were only distributed around some of the O, Ni, and Co in $LiMO_2$ structures. Thus, at high voltage (≥4.5 V), electrons were extracted not only from the non-bonding O2p state in Li_2MnO_3, but also from the Ni—O and Co—O bonds near the "phase-like interfaces B," which delivered electrons to participate in the oxidation reaction, increasing the reaction activity.

The L-edge of Ni and Co sXAS spectra during the charging states were obtained to confirm the conclusions of DFT calculations. The relative intensity of the main peak located at ≈852.9 eV and the weaker shoulder peak located at ≈855 eV can roughly correspond to the electronic state of the Ni element in the Ni L_{III} edge spectra.[26,28] As shown in Figure 4f, the weaker shoulder peak at higher energy ≈855 eV became higher and broadened from the pristine state to 4.4 V state upon sample L5, which corresponds to the oxidation of Ni to higher Ni^{3+} or Ni^{4+}. It was worth noting that with the increase in charging voltage, the intensity of the weak shoulder peak in the 4.8 V state has been further improved. Similarly, for the Co L-edge sXAS spectra, the slight shift to the higher energy range of the L_{III} main peak at ≈778.2 eV and the weak shoulder peak at ≈780.2 eV corresponds to the lifting in the oxidation state of Co.[9,29] As shown in Figure 4g, the slight shift of the peak position to the high-energy state during the Co L-edge spectra ran through the entire charging process. The above spectroscopic observations further confirm the DFT calculation conclusion that the dispersed distribution allows the generation of the complex electronic states in the complex structure, resulting in the appearance of higher energy 3d electrons and lower energy 2p electrons, which renders the high voltage activity of TM_{3d}-O_{2p}.

In addition to the changes in electronic structure, the dispersed distribution of the two structures also promoted the deintercalation ability of Li ions compared to the large-scale structure distribution that renders the reaction to be completely split into two isolated parts. In the low voltage range, the lithium ions in $LiMO_2$ structures were extracted, followed by the interlayer spacing expansion due to the repulsion between the oxygen layers. Profiting from the extremely dispersed composite of Li_2MnO_3 structure and $LiMO_2$ structure, the interlayer spacing of the Li_2MnO_3 structure was expanded in conjunction with the local expansion of the interlayer spacing in $LiMO_2$ after delithiation, thus promoting the migration of Li ions in Li_2MnO_3 structure during the high voltage range. We performed FIB processing on sample L5 at the first charging state of 4.4 V to show the bulk structure. HAADF-STEM image (Figure 3c,d) confirmed that the interlayer spacing (TM/$LiMn_2$ layer—TM/$LiMn_2$ layer) of all structures have been expanded despite the partial delithiation state of 4.4 V, from 4.8 to 5.0 Å. Pure Li_2MnO_3 materials have been shown to possess rather poor kinetic and (de)intercalation capabilities of Li ions, making it impossible to deliver the high theoretical capacity in reality. However, LRMO materials possess a completely different deintercalation ability of Li ions than pure Li_2MnO_3 materials, benefiting from the presence of the $LiMO_2$ structure and the dispersed composition of the $LiMO_2$ structure with the Li_2MnO_3 structure in the nanoscale. The synergistically expanded interlayer spacing promotes the deintercalation of the excess Li within the Li layer and $LiMn_2$ layer.

The Rietveld refinements of the three pristine samples were applied in an attempt to eliminate the Li-ions transport behavior affected by the TM ions in Li layers. The results of Rietveld refinements were listed in Figure S5 and Table S2, Supporting Information, the value of "TM ions in Li layers" was not significantly different among the three samples. In addition, the electrochemical impedance spectroscopy (EIS) for different charging states during the first charge was added, and we selected three samples for each charging state which charged to cutoff voltages of 4.4 V (before the plateau), 4.5 V (at the early stage of the plateau), 4.55 V (at the middle stage of the plateau), and 4.6 V (after the plateau) for EIS. The relevant fitting and calculation results and equivalent circuits were shown in Table S3 and Figure S6, Supporting Information. The R_e (ohmic impedance) for different samples in different states of charge was relatively similar, demonstrating that the electron transport in the electrode was not affected by the changes in material structure. Strikingly, despite the gradual increase of the first charge capacity from sample L0 to L5, the R_{ct} (charge transfer impedance) of L0 was much higher than that of L5 at all four charging states and showed a significant decrease trend from L0 to L3 to L5. The sharp increase in charging as well as plateau capacity corresponded to the smaller R_{ct}, implying the intrinsic charge transfer enhanced by the complexity of the local structure distribution is inextricably linked to the improvement of capacity as well as anionic activity. Moreover, galvanostatic intermittent titration technique (GITT) tests for the first charge/discharge process of the three samples were employed to describe the kinetic process of ion transport. GITT curves for the first cycle of the three samples were shown in Figure S7c, Supporting Information, and the Figure S7a,b, Supporting Information, illustrated the distribution of the Li-ion diffusion coefficient versus specific capacity calculated by GITT. The diffusion coefficients showed a trend from higher to lower from sample L0 to sample L5 throughout the whole first charge/discharge process. The significant decrease of the diffusion coefficient from L0 to L3 to L5 samples during the lower charging range corresponded to the fact that the dispersed distribution also promoted the migration kinetics of Li ions in the $LiMO_2$ structure, that is, the dispersed distribution promoted more Li ions to be deintercalated in the $LiMO_2$ structure under the same current density, which was also connected with the increase of the interlayer spacing at 4.4 V. After low-voltage charging, as we have observed in STEM, the Li-ion migration kinetics in the nanoscale-dispersed Li_2MnO_3 structure was boosted, also reflected in the trend of improvement for Li-ion diffusion coefficient from L0 to L3 to L5 during the higher charging range. However, the GITT tests were performed at a very slow reaction rate for Li-ion (de)intercalation, and the resulting charge/discharge specific capacity is capable of excluding the effects from migration kinetics, but there was still a certain difference in the capacity for three samples delivered in the GITT tests (Figure S7c, Supporting Information). Therefore, in summary, the capacity difference caused by the change of distribution characteristics was essentially promoted by thermodynamics and dynamics. In addition, the anionic reaction process is closely related to the kinetic reaction,[9] which is not only

reflected in the diffusion promotion in the high voltage range of charging. In the trend of diffusion coefficients during the discharge process (Figure S7b, Supporting Information), the diffusion coefficients of the dispersed distribution structure were superior across the whole process, especially in the range of 3.0–3.5 V, which was the reaction corresponding to the oxygen reduction,[9,30] and hence the dispersed distribution promoted the slow kinetic process corresponding to the anionic reaction even in the discharge. Also, at a very slow reaction rate for GITT tests, the great increase in capacity during the 3.0–3.5 V range for discharge indicated the role of the thermodynamic co-promotion for the anionic reaction.

The ex-situ XRD curves that charged to cutoff voltages of 4.4 V (before the plateau), 4.5 V (at the early stage of the plateau), 4.55 V (at the middle stage of the plateau), and 4.6 V (after the plateau) for three samples were presented in the Figure S8, Supporting Information, and the corresponding refinement results were listed in the Table S4 and Figure S9, Supporting Information. After charging during the low voltage range before the plateau, a and b underwent slight shrinking deriving from the oxidation of transition metals, while c of all three samples got the greater increase corresponding to the expanding of the interlayer spacing. In agreement with that revealed above, more Li ions being extracted in the sample from L0 to L5 resulted in a stronger repulsion between oxygen layers and consequently a larger increase in the constant c. However, the sample possessing dispersed distribution characteristics at the nanoscale was found not to exhibit drastic lattice shrinking at the long-range scale after undergoing charging plateau as well as charge compensation of lattice oxygen. It benefits from the stabilizing effect of the dispersed distribution characteristics on the structure of the delithiated state, in this case the oxygen loss and the structural transition occur at the surface at the short-range scale, as captured by STEM, and the layer structure in the bulk is relatively well maintained.

2.2.2. Reversibility of Anionic Oxidation and Reduction as well as the Phenomenon of Voltage Hysteresis

Early theories suggested that the reaction of lattice oxygen in LRMO materials only involves the oxidation in the first charge without the subsequent reversible reduction or even the reaction over long cycles, and the Li and O were irreversibly extracted in the form of Li_2O. However, recent studies have shown that lattice oxygen was capable of being oxidized and reduced reversibly during the cycle with some intermediate structures to continue the reaction, although the mechanism of the reversible reaction is still in dispute.[31–33] In contrast, pure Li_2MnO_3 material possessed oxygen oxidation activity without reversible reactivity, which was confirmed in a recent study[34] due to the huge oxygen gas from the first charge. The reversibility mechanisms of anionic oxidation and reduction have been of strong interest. It was generally believed to be related to the formation of some intermediate structures in the material during the electrochemical processes, such as the reversible TM migration,[30] the O—O dimer,[32,33] and even the formation of molecular oxygen within the bulk,[31] and all these structures were pointed out to support the anionic reversibility.

The reversible behavior of oxidation and reduction for L0 with two structures distributed in isolation was similar to that of pure Li_2MnO_3 materials, as shown in Figure 3a, whose first coulomb efficiency was very low, possessing lower charging activity and the worse reversibility of lattice oxygen. The oxygen possessed strong irreversibility in the subsequent reduction process, and the overall reaction was more like the superposition of pure Li_2MnO_3 and pure $LiMO_2$ materials. While the uniformly dispersed composite of $LiMO_2$ structure and Li_2MnO_3 structure like sample L5 contributed LRMO materials to exhibit completely different reversible behaviors, especially oxygen oxidation and the recoverability of reduction.

The particles of sample L5 after the first full delithiation (4.8 V) were processed by FIB treatment and the STEM was used to display the structure changes at the atomic scale. The particles remained relatively intact after undergoing oxygen oxidation at high voltage and a large amount of delithiation (Figure S10b, Supporting Information, and Figure 3e). In addition to the thin phase transition on the surface, which was caused by the oxygen loss from the surface, and was also the explanation for the irreversible behavior during the initial cycle. The surface is the initial area for oxygen loss, causing a certain range of structure disorders and phase transitions, and is the beginning of structure degradation and voltage decay in LRMO materials. It was not as bad at the beginning of the cycle in the sample with dispersed distribution and was responsible for about ten percent of the irreversibility capacity. In contrast to the surface, as shown in Figures 3e and 4f, the bulk structures have been well maintained, with no oxygen release or severe structure transformation, which determines the reversible capacity of the material and the recoverability of the reduction reaction. The complete structures and Li—Mn—Mn ordering could be shown. The atomic arrangement in the bulk (Figure 3e) showed that the layered structure has been well maintained, thus ensuring the recoverability of the reduction reaction, which was attributed to the structure retention of Li_2MnO_3 by the dispersed $LiMO_2$ structure. For the isolated distribution of Li_2MnO_3 such as L0, the oxygen behavior is more like that of pure Li_2MnO_3 materials, where oxygen is released as gas after the oxygen oxidation as well as the extraction of lithium ions. The O formed a short O—O bond spontaneously in the structure of pure Li_2MnO_3 after delithiation, which was highly susceptible to release. However, it was not the case for the dispersed composite of $LiMO_2$ and Li_2MnO_3 in the bulk. The Li_2MnO_3 structure and the Li_2MnO_3 structure were separated by the dispersed $LiMO_2$ structure. It was difficult for Li_2MnO_3 to form oxygen condensation after Li extraction, and the highly oxidized oxygen can only be bound within the bulk lattice, as confirmed by the DFT calculations in Figure S10c, Supporting Information. Furthermore, as mentioned in detail above, the part of Ni e_g together with the t_{2g} orbital of Co reduced the energy and replaced part of activity from oxygen during high voltages, stabilizing the oxygen, which likewise contributed to the retention of the layered structures and the reaction recovery of lattice oxygen.

The dQ/dV curves (Figure 3b) of the first charge/discharge analyzed the voltage distribution of different redox reactions, and the samples with different structure distribution characteristics exhibited great differences among them. The dispersed distribution significantly enhanced the recovery of the

reduction, and the gradual enhancement of the reversibility during the discharge process mainly came from the capacity increase in the voltage range of 3.0–3.5 V, which corresponds to the range of voltage hysteresis from lattice oxygen.[9,30] It indicates that the reversibility between oxidation and reduction from anion is inextricably linked to the voltage hysteresis phenomenon. For a long time, voltage hysteresis is one of the perplexing phenomena of LRMO materials, which manifests itself as a mismatch of potential between the charging and discharging of the same redox pair, and the high-voltage reaction of lattice oxygen in the charge is transferred to a lower voltage range during discharging. The oxidation of oxygen corresponds to the extraction of the non-bonding O2p states, which leaves behind the unoccupied states that should be filled at high voltage during discharging. However, part of the oxygen reduction reacts at relatively low voltages (3.0–3.5 V), suggesting that the local structure maintaining reversibility changes the electronic configuration of the lattice oxygen, lifting the energy of the O2p unoccupied states and thus changing the reaction voltage of reduction. The O K-edge sXAS spectra of sample L5 at the first discharged-3.2 V state are shown in Figure 4e and Figure S11, Supporting Information. The integrated intensity for the pre-edge peaks has been partly retained, which verified that the oxygen reaction was hystered to a lower voltage range. The dispersed distribution of $LiMO_2$ and Li_2MnO_3 structures positively contributes to voltage hysteresis.

The electronic structure analysis was carried out for the delithiated configuration with the dispersed distribution. As shown in **Figure 5**, the complex composite of multiple structures led to the appearance of multiple local environments for oxygen after delithiation. The unoccupied states of these oxygens possessed a complex and continuous distribution, which was distributed in multiple energy ranges, and were even partly higher than the empty orbital of Ni. The sequence of reduction reactions from high to low voltage during the discharge corresponds to the filling of unoccupied states from near to far from the Fermi level. The energy level distribution of multiple oxygen states corresponds to the distribution of reduction from oxygen in multiple voltage ranges, even in low voltage, explaining the voltage hysteresis phenomenon. Furthermore, the HAADF-STEM image for the sample at the full charging state (4.8 V) observed that the Li-Mn-Mn ordering in some Li_2MnO_3 structures was broken and the TM migrated within the plane, as shown in Figure 3f. Recently, PG Bruce et al.[31] believe that the in-plane migration of TM during the deintercalation of lithium promotes the reversible generation of oxygen molecules within the lattice, which accounts for the voltage hysteresis phenomenon. Here, the dispersion and composite between the Li_2MnO_3 structures and the $LiMO_2$ structures greatly facilitated the in-plane migration of TM, thereby providing vacancies within the lattice capable of accommodating oxygen molecules, which in turn led to the occurrence of voltage hysteresis. On the whole, the voltage hysteresis phenomenon in LRMO materials is caused by several factors, and the thermodynamic factor caused by the changes in the electron structure in lattice oxygen is one of the essential causes of the voltage hysteresis phenomenon. The changes in the electronic structure of lattice oxygen are caused by a variety of changes in coordination environments, including the recombination of multiple structures and the formation of molecular oxygen within the bulk. The dispersed distribution of $LiMO_2$ and Li_2MnO_3 structures in the particles plays a decisive role in these changes of coordination environments and is the main factor for the formation of voltage hysteresis in LRMO materials. The reversibility of anionic redox as well as the probe during electrochemical processes in LRMO materials have evolved through many investigations in the past research, while the maintenance of the reversibility has also been discussed and emphasized such as TM migration, the O—O dimer, and even the formation of molecular oxygen within the bulk. The reaction in the voltage range of 3.0–3.5 V in discharge was confirmed for the reduction characteristics of oxygen.[9,30] In this work, the reversible reduction characteristics of oxygen were enhanced with the increase of dispersion as obtained in the slow GITT reaction as well as in the dQ/dV analysis of the first cycle, meanwhile the structure transitions that were capable of maintaining the reversibility of anionic reduction were captured in STEM. However, although the oxygen redox activity arising from the structure distribution was confirmed based on the available results, a definitive and quantitative oxygen redox reversibility changed by structure distribution is yet to be achieved. Therefore, the direct probe like resonant inelastic X-ray scattering regarding anionic redox is being further developed.

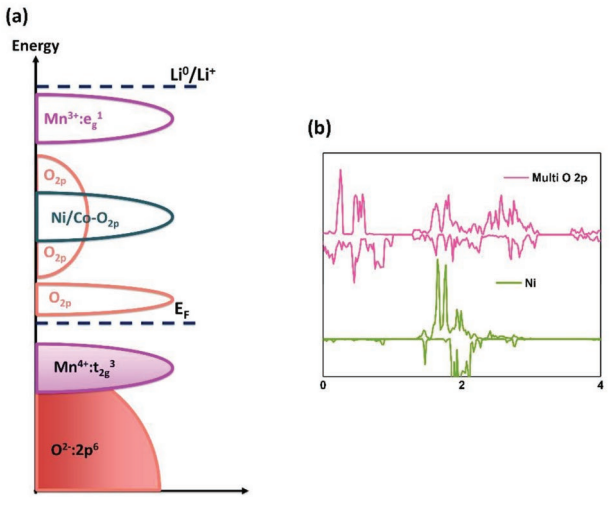

Figure 5. a) Schematic diagram of the electronic structure in the distribution of multiple complex structures after delithiation. b) O pDOS in the multiple local structures at the delithiated state and the pDOS of normal Ni.

3. Conclusions

In this work, we presented the concept of structure distribution in LRMO materials. Through the in-depth analysis from the atomic scale to electronic structure and reaction behavior, the distribution of Li_2MnO_3 and $LiMO_2$ phases was found to be the essential origin of the electrochemical reaction behavior in LRMO materials. The introduction of dispersibility contributes to a deeper understanding of the reactive behaviors, such as the strong activity of oxygen, the deintercalation ability of Li ions, the oxidation and reduction reversibility of anion, and the

explains of voltage hysteresis that has been troubling for a long time, and the voltage hysteresis is inseparable from the maintenance of the reversibility. Although the observations confirmed that the changes in synthesis conditions leaded to the complex structure distributions and hence affected electrochemical behavior, changes in the Li: TM ratio inevitably altered the compositions and alterations in the Li content also had an impact on the electrochemical behavior. Further work such as ensuring the composition ratio while changing other synthesis conditions like roasting temperature and time is being performed, resulting in a comparison of compounds with the same composition but different structure distribution characteristics

4. Experimental Section

Material Preparation: The transition metal (TM) carbonates precursor ($Mn_{0.54}Ni_{0.13}Co_{0.13}(CO_3)_{0.8}$ was prepared by a co-precipitation method. Stoichiometric $NiSO_4{\cdot}6H_2O$, $CoSO_4{\cdot}7H_2O$, and $MnSO_4{\cdot}H_2O$ were dissolved with a concentration of 1.0 mol L^{-1} as the starting solution, together with the aqueous solution of 2 mol L^{-1} Na_2CO_3, were titrated simultaneously by a peristaltic pump into the 20L continuously stirred tank reactor to react under 60 °C and constant pH of 8.0. The precipitation was obtained by constant stirring and evaporation, and the precipitation was centrifuged, filtered, washed, and dried to obtain the desired precursor ($Mn_{0.54}Ni_{0.13}Co_{0.13}(CO_3)_{0.8}$.

The precursors were mixed with different ratios of Li_2CO_3 and the sample names were named using the difference in the ratios of Li_2CO_3 to the precursors, that is, L0 (Li:TM ratio of 1.2:0.8, $Li_{1.2}Mn_{0.54}Ni_{0.13}Co_{0.13}O_2$), L3 ($Li_2CO_3$ mass reduction of 3%, Li:TM ratio of 1.164: 0.8), and L5 (Li_2CO_3 mass reduction of 5%, Li:TM ratio of 1.14: 0.8) . Then, the mixtures were calcinated in two stages in air, heated to 450 °C with a heating rate of 3 °C min^{-1} and calcined at 500 °C for 5 h, then heated to 850 °C and calcinated for 20 h.

X-Ray Diffraction and Refinement: XRD patterns were collected by the use of Rigaku SmartLab X-ray diffractometer with Cu Kα radiation between 10° and 120°.

Aberration Correction Scanning Transmission Electron Microscopy: All the cross sectional samples to be observed were treated with the FIB technique first to demonstrate the structures from the surface to the bulk. AC-STEM was performed using the FEI Titan Themis G3 electron microscope equipped with the HAADF detectors at the accelerating voltage of 300 kV.

X-Ray Absorption Spectroscopy: Soft XAS spectra of the O K-edge were collected at beamline BL02B02 in the Shanghai Synchrotron Radiation Facility, Shanghai, China. Soft XAS spectra of the Mn L-edge, Ni L-edge, and Co-edge were collected at beamline BL12B in the National Synchrotron Radiation Laboratory, Anhui, China.

Electrochemical Test: The CR2032 coin cell was used to test the electrochemical performance of the above cathode materials with lithium metal as the negative electrode. The positive electrode was made of 80 wt% LRMO sample, 10 wt% Super P, and 10 wt% polyvinylidene fluoride, and then coated on the surface of the aluminum foil. The mass-loading of active materials in the cathode is ≈4.0 mg cm^{-2}. The electrolyte consists of 1 M $LiPF_6$ in ethylene carbonate (EC) and diethyl carbonate, and Celgard 2500 was chosen as the separator. All the above components were assembled in the Ar-filled glove box. The galvanostatic tested between 2.0 and 4.8 V (vs Li/Li^+) were carried out by Land CT2001A at 25 °C.

Samples at different charged and discharged states for XRD, XAS, and AC-STEM tests were first charged or discharged to different states at a rate of 0.05C (10 mA g^{-1}), and then were disassembled in the glovebox, and washed thoroughly with DMC. They were maintained in a dry argon atmosphere, then were transferred from the argon glovebox to different tests (kept under vacuum).

First-Principle Calculations: All of the first-principle calculations were performed by the projector augmented wave method[35] based on the DFT,[36] as implemented the Vienna ab initio simulation package.[37] The strong correlation effect of Mn, Ni, and Co has been modified by the DFT with Hubbard U correction,[38,39] and the values of U-J for Mn, Ni, and Co ions were set to be 4.5, 6.2, and 3.32 eV, based on the spin-polarized generalized gradient approximation with the Perdew–Burke–Ernzerho exchange–correlation functional.[40] The model of each local structure has been described in detail in the text. The cutoff energy was set to be 520 eV. The total energy converged was set to be 10^{-5} eV and the final force on each atom is less than 0.05 eV $Å^{-1}$. The Monkhorst–Pack scheme[41] was selected in the Brillouin zone.

Supporting Information

Supporting Information is available from the Wiley Online Library or from the author.

Acknowledgements

H.Z. and H.P. contributed equally to this work. The authors acknowledge the help of the XAS experiments from the staff and the facility on Beamlines MCD-A and MCD-B (Soochow Beamline for Energy Materials) at National Synchrotron Radiation Laboratory (NSRL), and Beamlines BL02B02 at Shanghai Synchrotron Radiation Facility (SSRF). This research was supported by Beijing Natural Science Foundation (JQ22028), the National Youth Talent Support Program (SQ2022QB02427), Beijing Municipal Science & Technology Commission (Z221100006722017), GRINM Youth Foundation Funded Project (2022HX016), National Natural Science Foundation of China (52072282), National Natural Science Foundation of China (U1764255), National Natural Science Foundation of China (22005264), Guangdong Provincial Science and Technology Commission, Guangdong Key Areas R&D Program (2020B0909030004), and Guangdong High-level Innovation Institute Project (2021B0909050001).

Conflict of Interest

The authors declare no conflict of interest.

Data Availability Statement

The data that support the findings of this study are available from the corresponding author upon reasonable request.

Keywords

anion redox, electronic structure, lithium-rich cathodes, local structures, scanning transmission electron microscopy

Received: October 5, 2022
Revised: January 30, 2023
Published online:

[1] M. Fichtner, K. Edström, E. Ayerbe, M. Berecibar, A. Bhowmik, I. E. Castelli, S. Clark, R. Dominko, M. Erakca, A. A. Franco, A. Grimaud, B. Horstmann, A. Latz, H. Lorrmann, M. Meeus, R. Narayan, F. Pammer, J. Ruhland, H. Stein, T. Vegge, M. Weil, *Adv. Energy Mater.* **2022**, *12*, 2102904.
[2] M. Li, T. Liu, X. Bi, Z. Chen, K. Amine, C. Zhong, J. Lu, *Chem. Soc. Rev.* **2020**, *49*, 1688.

[3] H. Zhuo, A. Zhang, X. Huang, J. Wang, W. Zhuang, *Inorg. Chem. Front.* **2021**, *8*, 4590.
[4] W. Zuo, M. Luo, X. Liu, J. Wu, H. Liu, J. Li, M. Winter, R. Fu, W. Yang, Y. Yang, *Energy Environ. Sci.* **2020**, *13*, 4450.
[5] E. Hu, X. Yu, R. Lin, X. Bi, J. Lu, S. Bak, K.-W. Nam, H. L. Xin, C. Jaye, D. A. Fischer, K. Amine, X.-Q. Yang, *Nat. Energy* **2018**, *3*, 690.
[6] Z. Lu, D. MacNeil, J. Dahn, *Electrochem. Solid-State Lett.* **2001**, *4*, A191.
[7] D.-H. Seo, J. Lee, A. Urban, R. Malik, S. Kang, G. Ceder, *Nat. Chem.* **2016**, *8*, 692.
[8] G. Assat, J.-M. Tarascon, *Nat. Energy* **2018**, *3*, 373.
[9] G. Assat, D. Foix, C. Delacourt, A. Iadecola, R. Dedryvere, J. M. Tarascon, *Nat. Commun.* **2017**, *8*, 2219.
[10] P. Yan, J. Zheng, Z.-K. Tang, A. Devaraj, G. Chen, K. Amine, J.-G. Zhang, L.-M. Liu, C. Wang, *Nat. Nanotechnol.* **2019**, *14*, 602.
[11] J. Zheng, M. Gu, A. Genc, J. Xiao, P. Xu, X. Chen, Z. Zhu, W. Zhao, L. Pullan, C. Wang, J.-G. Zhang, *Nano Lett.* **2014**, *14*, 2628.
[12] M. Gu, A. Genc, I. Belharouak, D. Wang, K. Amine, S. Thevuthasan, D. R. Baer, J.-G. Zhang, N. D. Browning, J. Liu, C. Wang, *Chem. Mater.* **2013**, *25*, 2319.
[13] J. Zheng, M. Gu, J. Xiao, P. Zuo, C. Wang, J.-G. Zhang, *Nano Lett.* **2013**, *13*, 3824.
[14] S. Hu, Y. Li, Y. Chen, J. Peng, T. Zhou, W. K. Pang, C. Didier, V. K. Peterson, H. Wang, Q. Li, Z. Guo, *Adv. Energy Mater.* **2019**, *9*, 1901795.
[15] P. M. Csernica, S. S. Kalirai, W. E. Gent, K. Lim, Y.-S. Yu, Y. Liu, S.-J. Ahn, E. Kaeli, X. Xu, K. H. Stone, A. F. Marshall, R. Sinclair, D. A. Shapiro, M. F. Toney, W. C. Chueh, *Nat. Energy* **2021**, *6*, 642.
[16] C. R. Fell, K. J. Carroll, M. Chi, Y. S. Meng, *J. Electrochem. Soc.* **2010**, *157*, A1202.
[17] Y. Li, S. Xu, W. Zhao, Z. Chen, Z. Chen, S. Li, J. Hu, B. Cao, J. Li, S. Zheng, Z. Chen, T. Zhang, M. Zhang, F. Pan, *Energy Storage Mater.* **2022**, *45*, 422.
[18] J. Hwang, S. Myeong, E. Lee, H. Jang, M. Yoon, H. Cha, J. Sung, M. G. Kim, D.-H. Seo, J. Cho, *Adv. Mater.* **2021**, *33*, 2100352.
[19] T. Liu, J. Liu, L. Li, L. Yu, J. Diao, T. Zhou, S. Li, A. Dai, W. Zhao, S. Xu, Y. Ren, L. Wang, T. Wu, R. Qi, Y. Xiao, J. Zheng, W. Cha, R. Harder, I. Robinson, J. Wen, J. Lu, F. Pan, K. Amine, *Nature* **2022**, *606*, 305.
[20] H. Yu, Y.-G. So, A. Kuwabara, E. Tochigi, N. Shibata, T. Kudo, H. Zhou, Y. Ikuhara, *Nano Lett.* **2016**, *16*, 2907.
[21] H. Yu, R. Ishikawa, Y. G. So, N. Shibata, T. Kudo, H. Zhou, Y. Ikuhara, *Angew. Chem., Int. Ed.* **2013**, *52*, 5969.
[22] J. Bareño, M. Balasubramanian, S. H. Kang, J. G. Wen, C. H. Lei, S. V. Pol, I. Petrov, D. P. Abraham, *Chem. Mater.* **2011**, *23*, 2039.
[23] A. S. Menon, S. Ulusoy, D. O. Ojwang, L. Riekehr, C. Didier, V. K. Peterson, G. Salazar-Alvarez, P. Svedlindh, K. Edström, C. P. Gomez, W. R. Brant, *ACS Appl. Energy Mater.* **2021**, *4*, 1924.
[24] J. Hwang, S. Myeong, W. Jin, H. Jang, G. Nam, M. Yoon, S. H. Kim, S. H. Joo, S. K. Kwak, M. G. Kim, J. Cho, *Adv. Mater.* **2020**, *32*, 2001944.
[25] Y. Peng, P. D. Nellist, S. J. Pennycook, *J. Electron Microsc.* **2004**, *53*, 257.
[26] W. S. Yoon, M. Balasubramanian, K. Y. Chung, X. Q. Yang, J. Mcbreen, C. P. Grey, D. A. Fischer, *J. Am. Chem. Soc.* **2005**, *127*, 17479.
[27] K. Luo, M. R. Roberts, R. Hao, N. Guerrini, D. M. Pickup, Y.-S. Liu, K. Edström, J. Guo, A. V. Chadwick, L. C. Duda, P. G. Bruce, *Nat. Chem.* **2016**, *8*, 684.
[28] W.-S. Yoon, M. Balasubramanian, X.-Q. Yang, Z. Fu, D. A. Fischer, J. McBreen, *J. Electrochem. Soc.* **2004**, *151*, A246.
[29] M. Oishi, C. Yogi, I. Watanabe, T. Ohta, Y. Orikasa, Y. Uchimoto, Z. Ogumi, *J. Power Sources* **2015**, *276*, 89.
[30] W. E. Gent, K. Lim, Y. Liang, Q. Li, T. Barnes, S. Ahn, K. H. Stone, M. Mcintire, J. Hong, J. Song, *Nat. Commun.* **2017**, *8*, 2091.
[31] R. A. House, G. J. Rees, M. A. Pérez-Osorio, J. J. Marie, P. G. Bruce, *Nat. Energy* **2020**, *5*, 777.
[32] X. Li, Y. Qiao, S. Guo, Z. Xu, H. Zhu, X. Zhang, Y. Yuan, P. He, M. Ishida, H. Zhou, *Adv. Mater.* **2018**, *30*, 1705197.
[33] E. Zhao, M. Zhang, X. Wang, E. Hu, J. Liu, X. Yu, M. Olguin, T. A. Wynn, Y. S. Meng, K. Page, *Energy Storage Mater.* **2020**, *24*, 384.
[34] J. Rana, J. K. Papp, Z. Lebens-Higgins, M. Zuba, L. A. Kaufman, A. Goel, R. Schmuch, M. Winter, M. S. Whittingham, W. Yang, B. D. McCloskey, L. F. J. Piper, *ACS Energy Lett.* **2020**, *5*, 634.
[35] G. Kresse, D. P. Joubert, *Phys. Rev. B* **1999**, *59*, 1758.
[36] W. Kohn, L. J. Sham, *Phys. Rev.* **1965**, *140*, A1133.
[37] G. Kresse, J. Furthmuller, *Comput. Mater. Sci.* **1996**, *6*, 15.
[38] V. I. Anisimov, J. Zaanen, O. K. Andersen, *Phys. Rev. B* **1991**, *44*, 943.
[39] V. I. Anisimov, F. Aryasetiawan, A. I. Lichtenstein, *J. Phys.: Condens. Matter* **1997**, *9*, 767.
[40] J. P. Perdew, J. A. Chevary, S. H. Vosko, K. A. Jackson, M. R. Pederson, D. J. Singh, C. Fiolhais, *Phys. Rev. B* **1992**, *46*, 6671.
[41] H. J. Monkhorst, J. D. Pack, *Phys. Rev. B* **1976**, *13*, 5188.